Correction

ENGINEERING

Correction for "Computer simulations suggest that prostate enlargement due to benign prostatic hyperplasia mechanically impedes prostate cancer growth," by Guillermo Lorenzo, Thomas J. R. Hughes, Pablo Dominguez-Frojan, Alessandro Reali, and Hector Gomez, which was first published January 7, 2019; 10.1073/pnas.1815735116 (*Proc. Natl. Acad. Sci. U.S.A.* **116**, 1152–1161).

The authors note that Eq. **1** on page 1158 appeared incorrectly. The corrected equation appears below.

$$\frac{\partial \phi}{\partial t} = \nabla \cdot \left(M D_{\phi} \nabla \phi \right) + M \left(\chi s - A\phi - \frac{1}{\tau} \frac{\mathrm{d}F(\phi)}{\mathrm{d}\phi} \right)$$

Published online June 10, 2019.

www.pnas.org/cgi/doi/10.1073/pnas.1908514116

Computer simulations suggest that prostate enlargement due to benign prostatic hyperplasia mechanically impedes prostate cancer growth

Guillermo Lorenzo[a,b,1], Thomas J. R. Hughes[c,1], Pablo Dominguez-Frojan[d], Alessandro Reali[b], and Hector Gomez[d]

[a]Departamento de Matemáticas, Universidade da Coruña, 15071 A Coruña, Spain; [b]Department of Civil Engineering and Architecture, University of Pavia, 27100 Pavia, Italy; [c]Institute for Computational Engineering and Sciences, The University of Texas at Austin, Austin, TX 78712-1229; and [d]School of Mechanical Engineering, Purdue University, West Lafayette, IN 47907

Contributed by Thomas J. R. Hughes, October 30, 2018 (sent for review September 13, 2018; reviewed by Krishna Garikipati and Ellen Kuhl)

Prostate cancer and benign prostatic hyperplasia are common genitourinary diseases in aging men. Both pathologies may coexist and share numerous similarities, which have suggested several connections or some interplay between them. However, solid evidence confirming their existence is lacking. Recent studies on extensive series of prostatectomy specimens have shown that tumors originating in larger prostates present favorable pathological features. Hence, large prostates may exert a protective effect against prostate cancer. In this work, we propose a mechanical explanation for this phenomenon. The mechanical stress fields that originate as tumors enlarge have been shown to slow down their dynamics. Benign prostatic hyperplasia contributes to these mechanical stress fields, hence further restraining prostate cancer growth. We derived a tissue-scale, patient-specific mechanically coupled mathematical model to qualitatively investigate the mechanical interaction of prostate cancer and benign prostatic hyperplasia. This model was calibrated by studying the deformation caused by each disease independently. Our simulations show that a history of benign prostatic hyperplasia creates mechanical stress fields in the prostate that impede prostatic tumor growth and limit its invasiveness. The technology presented herein may assist physicians in the clinical management of benign prostate hyperplasia and prostate cancer by predicting pathological outcomes on a tissue-scale, patient-specific basis.

prostate cancer | benign prostatic hyperplasia | mathematical oncology | patient-specific | isogeometric analysis

Despite its small size and supporting role in the male genitourinary system, the prostate is the site of two major pathologies in older men: prostate cancer (PCa) and benign prostatic hyperplasia (BPH) (1). PCa is almost always an adenocarcinoma, a form of cancer that originates in epithelial tissues with glandular organization, for instance, the prostatic tissue in charge of producing certain substances of semen. Currently, PCa is the second most common cancer and the fifth leading cause of death from cancer in men worldwide, with an estimated 1.1 million new cases and 307,000 deaths in 2012 (2). PCa is usually diagnosed and treated when it is still localized within the prostate (1). The majority of PCa cases originate in the peripheral zone (PZ) of the prostate (70%), but PCa can also arise in the transition zone (20%) and in the central zone (10%). BPH consists of the pathological enlargement of the prostate with age, with a prevalence increasing from 50% in men in their 50s to about 70% in men in their 70s (3). This condition may arise in the transition zone or the periurethral glands (1). The growing tissue may obstruct urinary and ejaculatory flow, hence causing bothersome lower-urinary tract symptoms. As BPH does not develop in the PZ, the glandular prostate is segmented into two zones in radiological studies: the PZ and the central gland (CG), which contains the central, transition, and periurethral zones (1, 4, 5). The CG has a larger and denser stromal component that becomes more compact during BPH, which results in an overall lower signal intensity in T2-weighted magnetic resonance (MR) images. However, the signal intensity of the CG is usually rather heterogeneous due to the varying proportions of stromal and glandular hyperplasia (1, 4–7).

Beyond anatomical location, BPH and PCa possess other similarities (1, 8, 9). At the epidemiological level, both diseases affect older men, have increasing incidence with age, and frequently coexist in the same patient. These pathologies may induce lower-urinary tract symptoms and increase serum levels of prostatic specific antigen (PSA), a prostate activity biomarker used in PCa diagnosis and staging. Additionally, PCa and BPH share some genetic alterations, are hormone dependent, have been correlated with prior inflammation, and might be part of the metabolic syndrome. Despite the evidence suggesting links between PCa and BPH, the relationship between these diseases has been under continuous debate in the medical community due to the existence of contradictory studies and the scarcity of research thoroughly confirming the proposed hypothetical links (8, 9). Gaining knowledge about the connection between PCa and BPH would challenge the current clinical standards and potentially enhance treatment and prevention of both diseases.

Significance

Benign prostatic hyperplasia (BPH) is a common disease in aging men that causes the prostate to enlarge progressively. Men with larger prostates tend to harbor prostatic tumors with more favorable features. The underlying mechanisms that explain this interaction between BPH and prostate cancer (PCa) are largely unknown. Here, we propose that BPH may mechanically impede PCa growth by producing increasingly intense mechanical stresses in the prostate over time, which are known to slow down tumor dynamics. To explore this hypothesis, we ran a qualitative simulation study using an extension of our mathematical model of PCa growth including the mechanical deformation of the prostate under BPH and PCa. The proposed mechanism suggests relevant shifts in clinical management of PCa and BPH.

Author contributions: G.L., T.J.R.H., A.R., and H.G. designed research; G.L., T.J.R.H., A.R., and H.G. performed research; G.L., P.D.-F., and H.G. contributed new reagents/analytic tools; G.L., T.J.R.H., A.R., and H.G. analyzed data; and G.L., T.J.R.H., A.R., and H.G. wrote the paper.

Conflict of interest statement: H.G., T.J.R.H., and G.L. are listed as coinventors in a patent application that has been filed by The University of Texas at Austin. The invention leverages part of the technology presented in this paper.

Reviewers: K.G., University of Michigan; and E.K., Stanford University.

[1]To whom correspondence may be addressed. Email: hughes@ices.utexas.edu or guillermo.lorenzo@unipv.it.

This article contains supporting information online at www.pnas.org/lookup/suppl/doi:10.1073/pnas.1815735116/-/DCSupplemental.

Published online January 7, 2019.

The biopsy detection rate of PCa in large prostates is known to be lower than in small prostates (10–12). This low detection rate has been attributed to various artifacts, such as sampling errors and a biopsy selection bias in patients with increasing PSA, possibly caused by BPH (10, 13, 14). However, it appears that neither increasing sampling nor using more advanced medical imaging to perform biopsy has leveled the detection rate across prostate volume groups (11, 12, 15, 16). Recent studies on large series of radical prostatectomy specimens show that tumors arising in larger prostates present favorable pathological features, such as lower aggressiveness measured with the Gleason score (1), smaller tumor volume, and lower risk of extraprostatic extension or seminal vesicle invasion (10, 17–21). These studies provide solid evidence to suggest that large prostates may exert a protective effect against PCa, but the underlying mechanisms are not known.

Here, we propose a mechanical explanation for this phenomenon: BPH exerts an inhibitory effect on PCa growth due to the accumulation of mechanical stress. The rapid overproliferation of cancerous cells leads to high cell densities in their confined microenvironment within the harboring tissue. As a result, tumors develop a high compressive hydrostatic stress state in their interiors and exert outward forces as they grow. These forces deform the neighboring tissues, generating stress fields aimed at resisting the mechanical load imposed by tumor growth. This phenomenon is known as the tumor mass effect (22–28). In turn, these mechanical stress fields are known to exert an inhibitory effect on tumor growth both directly, by slowing down tumor dynamics, and indirectly, by deforming and collapsing the local vasculature in the tumor region. BPH creates a compressive hydrostatic stress state within the CG and outward forces that deform the PZ (1, 4, 5). Additionally, the confinement of the prostate in the pelvic area further contributes to the internal mechanical stress fields because the surrounding tissues resist the pathological deformation of this organ. Here, we show that, as the CG enlarges over time, the mechanical stress fields created by BPH intensify and reach larger values than those created by the tumor itself. Hence, BPH may also exert an inhibitory effect on PCa growth but its impact has been overlooked. Indeed, if clinically validated, this mechanism may produce a major change in BPH treatment. The current paradigm aims at reducing the CG volume to alleviate BPH symptoms via surgery or medication (1). According to the proposed mechanism, this would reduce the mechanical stresses in the prostate and hence promote the growth of coexisting PCa. This would put the patient in a dangerous predictive scenario, especially if the tumor was not previously diagnosed.

To analyze whether enlarged prostates may provide protection against PCa growth, we need to determine whether the stress induced by BPH is enough to significantly produce an inhibitory effect on PCa. This fundamentally requires a 3D, anatomically faithful, mechanical model of the prostate. The amount by which the growth rate of the tumor decreases with stress may be estimated from experiments in the literature. To perform this study, we derive a tissue-scale, patient-specific mechanically coupled mathematical model for PCa growth and perform a series of computer simulations. The study and design of mathematical models to forecast the evolution of tumors using computer simulations have given rise to the field of mathematical oncology (29–31). These models aim at complementing the current clinical practice in oncology by assisting physicians in better estimating disease progression and designing optimal treatment schemes. In particular, several mathematical models have incorporated the tumor mass effect to improve the prediction of the growth of various types of cancers (32–38). Fig. 1 depicts the geometry of the prostate used in our simulations, which we extracted from the MR images and anatomical segmentations of a patient suffering from PCa and BPH.

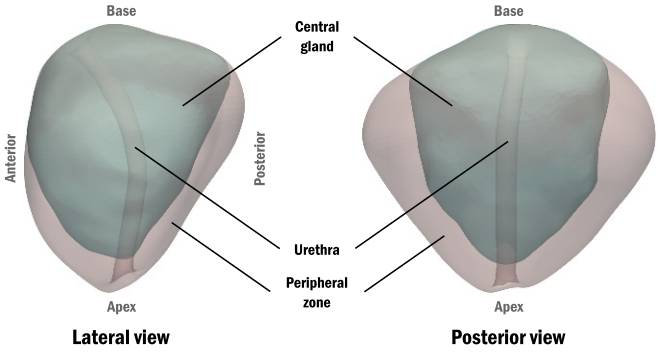

Fig. 1. Patient-specific local anatomy of the prostate. From a radiological perspective, the prostate is divided into central gland (CG) and peripheral zone (PZ). BPH takes place in the CG and most cases of PCa arise in the PZ. We extracted the geometry of the patient's prostate and CG from their corresponding segmentations provided on axial T2-weighted MR images. The volumes of the prostate, CG, and PZ at MRI date are 52.81 cc, 33.15 cc, and 19.66 cc, respectively. The major diameters of the prostate at MRI date have a length of 53.49 mm, 38.35 mm, and 52.01 mm in lateral, anteroposterior, and craniocaudal directions, respectively.

In this work, we extend our previous model of organ-confined PCa growth (39, 40) to include the equations of mechanical equilibrium and define the coupling terms between them and tumor dynamics. As organ-confined PCa growth can be seen as an evolving interface problem, we leverage the phase-field method (41) to account for the coupled dynamics of healthy and tumoral tissue. Our model also estimates PSA dynamics at tissue level by computing the serum concentrations of this biomarker produced at healthy and cancerous regions per unit volume of prostatic tissue (39). Following previous mechanically coupled approaches (32–38), we assume that the deformation of the prostate is a quasistatic phenomenon and we model prostatic tissue as a linear elastic, heterogeneous, isotropic material. As CG is normally stiffer than PZ in older men, we set a higher Young modulus in the CG (1, 4–7, 42–45). The confinement of the prostate in the pelvic region is modeled with Winkler-inspired boundary conditions on the external surface of the organ, while free displacement is imposed along the urethra. BPH and PCa are modeled as pressure terms in the constitutive equation of the prostatic tissue acting within the CG and the tumor, respectively. Finally, the inhibitory effect of the mechanical stress fields is estimated with a global factor that slows down tumor dynamics. This coefficient depends on a measure of the loading conditions and the stored elastic energy, so we choose a combination of the Von Mises stress and the hydrostatic stress for this purpose (46). The range of values of this inhibitory factor is adjusted to match the experimental and clinical observations in previous studies of tumor growth (23–28, 32–35). See *Materials and Methods* for more details on the model.

Results

Deformation of the Prostate Due to BPH. Our model predicted that BPH produces the volumetric expansion of the prostate in the perpendicular direction to the CG border, as depicted in Fig. 2 (*SI Appendix*, Fig. S1). The PZ was pushed outward from the borders of the growing CG against the prostate external surface and experienced a very slight shrinkage, as the boundary conditions partially enabled outward displacement.

The extremal values of the displacements were attained at the CG borders that are closer to the external surface of the prostate. The maximum total displacement was 0.74 mm. The urethra was displaced posteriorly and its diameter was virtually unaltered.

The hydrostatic stress was compressive within the CG (−0.20 kPa to −0.13 kPa) and negligible within the PZ (*SI*

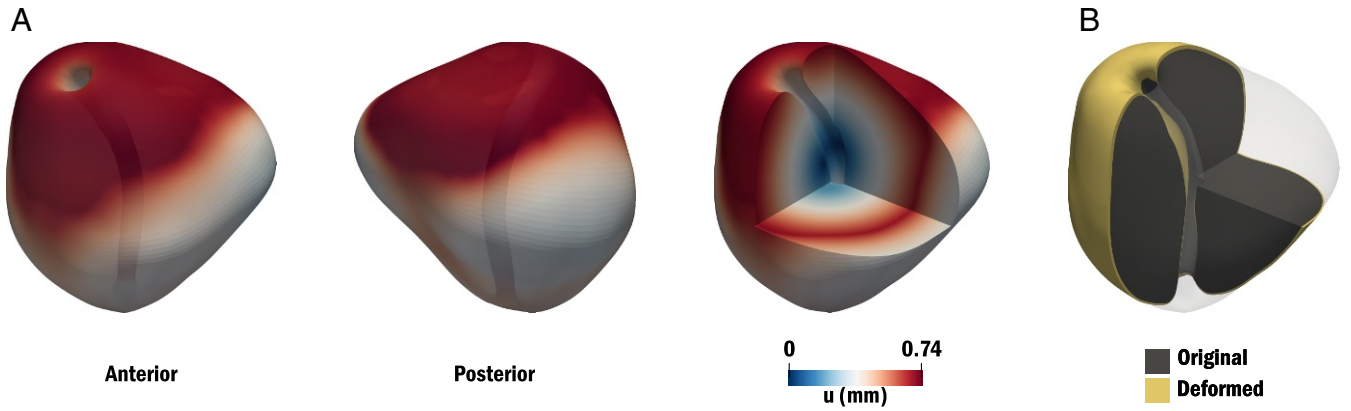

Fig. 2. Deformation of the prostate caused by BPH over 1 y. (*A*) Length of the displacement field vector over original anatomy at $t = 1$ y. (*B*) Original and deformed geometries of the prostate at $t = 1$ y.

Appendix, Fig. S1). Positive hydrostatic stress appeared in thin PZ regions between the CG border and the prostate boundary, where tension accumulated as the CG expanded. The Von Mises stress was negligible within the CG, except along the urethra (0.27–0.53 kPa). Within the PZ, the Von Mises stress peaked near the borders of the CG (0.20–0.33 kPa) and decreased toward the external surface of the prostate (0.07–0.17 kPa), depending on the distance between them (*SI Appendix*, Fig. S1).

Deformation of the Prostate Due to PCa. We considered three artificial tumors placed in characteristic locations within the prostate: the basal PZ, the apical PZ, and the CG. Each tumor had ellipsoidal geometry with one semiaxis measuring 4 mm and the others 3 mm. The largest dimension was oriented in anteroposterior direction. We selected the parameters that regulate tumor dynamics so that these tumors were aggressive and showed the typical morphologies of localized PCa: massive and fingered (39). Fig. 3 shows the growth of these artificial tumors and how they deformed the patient's prostate (*SI Appendix*, Fig. S2).

All tumors started growing with the massive morphology, which is characteristic of small prostatic cancers. The PZ tumors soon adjusted their geometry to the anatomy of the patient's prostate boundary (Fig. 3 *A1* and *A2* at $t = 0.3$ y). Due to the reduced thickness of the PZ around the CG in the patient's prostate, these PZ tumors invaded the CG early ($t < 0.1$ y). The CG tumor took longer to reach the PZ and invade it ($t \approx 0.3$ y). As every tumor grew in size, the intratumoral nutrient concentration decreased. This shortage cued a shape instability that progressively adjusted the tumors to a fingered or lobular morphology, hence ensuring a spatial distribution of nutrient that sustained tumor growth (39). This phenomenon happened by $t = 0.4$ y for the tumor in basal PZ, by $t = 0.35$ y for the tumor in apical PZ, and by $t = 0.55$ y for the CG tumor. The shift in morphology arrested tumor growth momentarily (<0.15 y) and even reduced the CG tumor volume by 12.2%. However, tumors grew faster and more extensively after this phenomenon.

The CG tumor grew faster and larger than the PZ tumors, whose growth rates and initial volumes were similar. Because the tumor in apical PZ underwent the change in morphology earlier, its volume was larger than that of the basal PZ tumor for the second half of the simulation. The final volumes of the basal PZ tumor, the apical PZ tumor, and the CG tumor were 5.43 cc, 6.82 cc, and 9.02 cc, respectively.

Tumors produced a local swelling deformation. The outermost tumoral structures produced the greatest displacements, which ranged between 0.65 mm and 1.15 mm and created noticeable smooth lumps on the external prostatic boundary, especially in the PZ (Fig. 3 *B1*, *B3*, *C1*, and *C3* and *SI Appendix*, Fig. S2). The CG tumor barely deformed the posterior aspect of the PZ. During the shift in tumor morphology, the displacement fields redistributed and decreased globally between 23% and 31%, taking 0.3–0.6 y to recover during fingered growth. The urethra was displaced away from the tumor and also constricted (max. 0.44–0.75 mm), mainly in the segments circumvented by the fingered tumors.

The hydrostatic stress was compressive within the tumors, with lower values in the PZ (-0.75 kPa to -0.33 kPa; *SI Appendix*, Fig. S2). Around the tumors, the hydrostatic stress was compressive in the PZ, with a minimum of -0.08 kPa, and tensile in the CG, with a maximum of 0.10 kPa. Maximal tensile hydrostatic stress between 0.67 kPa and 0.88 kPa was obtained on the most constricted contours of the urethra and was accompanied by compressive values with minimum between -0.52 kPa and -0.38 kPa on the urethral contours in a perpendicular direction to the constriction. High tensile hydrostatic stress was also registered when tumors grew near the prostate external surface (up to 0.33 kPa in PZ and 0.48 kPa in CG). Far from the tumor, the hydrostatic stress was negligible.

The Von Mises stress ranged between 0.05 kPa and 0.25 kPa inside the tumor and it was higher around the convex side of the tumor borders, with values typically between 0.45 kPa and 0.60 kPa (*SI Appendix*, Fig. S2). Maximal values of the Von Mises stress were obtained in the healthy tissue between tumor branches (0.60–0.70 kPa), within intricate concave regions of fingered tumors (0.60–0.75 kPa), within and around the tumor near the border between the PZ and the CG (0.41–0.87 kPa), in healthy tissue compressed by the tumor against the prostate external surface (0.50–0.92 kPa), and on the contour of the most constricted segments of the urethra (0.75–1.27 kPa). The healthy tissue enclosed by tumor branches had Von Mises stress values within the intratumoral range. Massive tumors tended to build up greater values of the Von Mises stress around them. We observed that the Von Mises stress was slightly higher and the distortion rim was thicker in the CG.

BPH Impedes PCa Growth. After the deformational study of the prostate under the effect of BPH and PCa to calibrate our model, we analyzed how the patient's history of BPH affected PCa growth. We ran two simulations: one without considering BPH and another including it. Fig. 4 depicts the growth of the tumor in both scenarios, while Fig. 5 shows the deformational states (*SI Appendix*, Figs. S3 and S4). The geometry of the patient's tumor was extracted from the same MR dataset used to obtain the prostate anatomy. We estimated the stress state

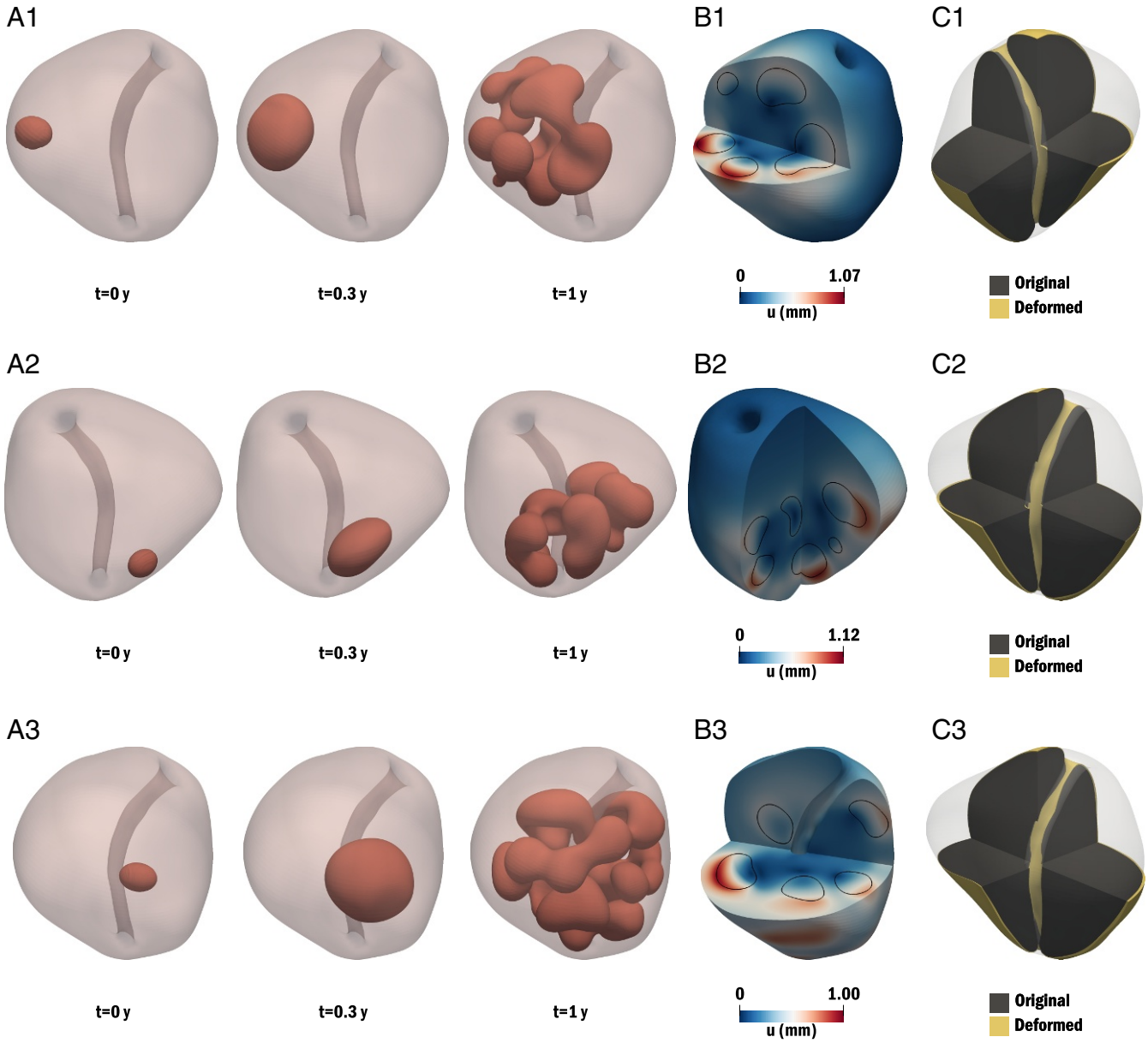

Fig. 3. Deformation of the prostate over 1 y produced by a tumor originated on basal PZ (*A1–C1*), apical PZ (*A2–C2*), and median CG (*A3–C3*). (*A1–A3*) Tumor growth over the original prostate geometry. (*B1–B3*) Length of the displacement field vector over original anatomy at $t = 1$ y. The contour of the tumor is depicted with black curves. (*C1–C3*) Original and deformed geometries of the prostate at $t = 1$ y.

of the prostate caused by years of developing BPH before PCa detection at the MR date, $\boldsymbol{\sigma}^0$. This information was introduced as a prestress to compute the baseline hydrostatic and Von Mises stresses in the mechanotransductive coefficient adjusting tumor dynamics (*Materials and Methods*). Hence, for this purpose, $\boldsymbol{\sigma} = \boldsymbol{\sigma}^0 + \boldsymbol{\sigma}^1$, where $\boldsymbol{\sigma}^1$ represents the additional stresses developed since the detection of PCa at MR date. All stress values quoted are for $\boldsymbol{\sigma}$.

The simulation without BPH rendered similar results to the PZ tumor cases in the previous section. The patient's tumor was located in the left basal aspect of the PZ and had a volume of 0.51 cc. Initially, this tumor grew with massive morphology, early invading the CG and progressively developing two lobes of preferential growth in the anteroposterior direction. This geometry contributed to an early shift in morphology between $t = 0.3$ y and $t = 0.4$ y, during which tumor growth was minimally slowed down. Afterward, the tumor grew faster with fingered morphology, invading all of the prostate side where it had originated from median to basal height in the craniocaudal direction.

The final volume of the tumor was 6.32 cc. The urethra was displaced anteriorly to the patient's right and the maximal constriction was 0.30 mm. The distribution and magnitude of the displacement, hydrostatic stress, and Von Mises stress fields were also analogous to their counterparts in the simulations for the PZ tumors in the previous section. The maximum total displacements were in the range 0.85–1.05 mm. The shape instability reduced displacements by 17.3% and it took until the end of the simulation for them to recover ($t \approx 0.9$).

The inclusion of the patient's history of BPH produced major changes in tumor growth and the prostate deformational state. There was no shift in morphology in this simulation. Instead, the tumor grew as a continuous mass that progressively surrounded the CG in the anteroposterior direction at the basal level of the

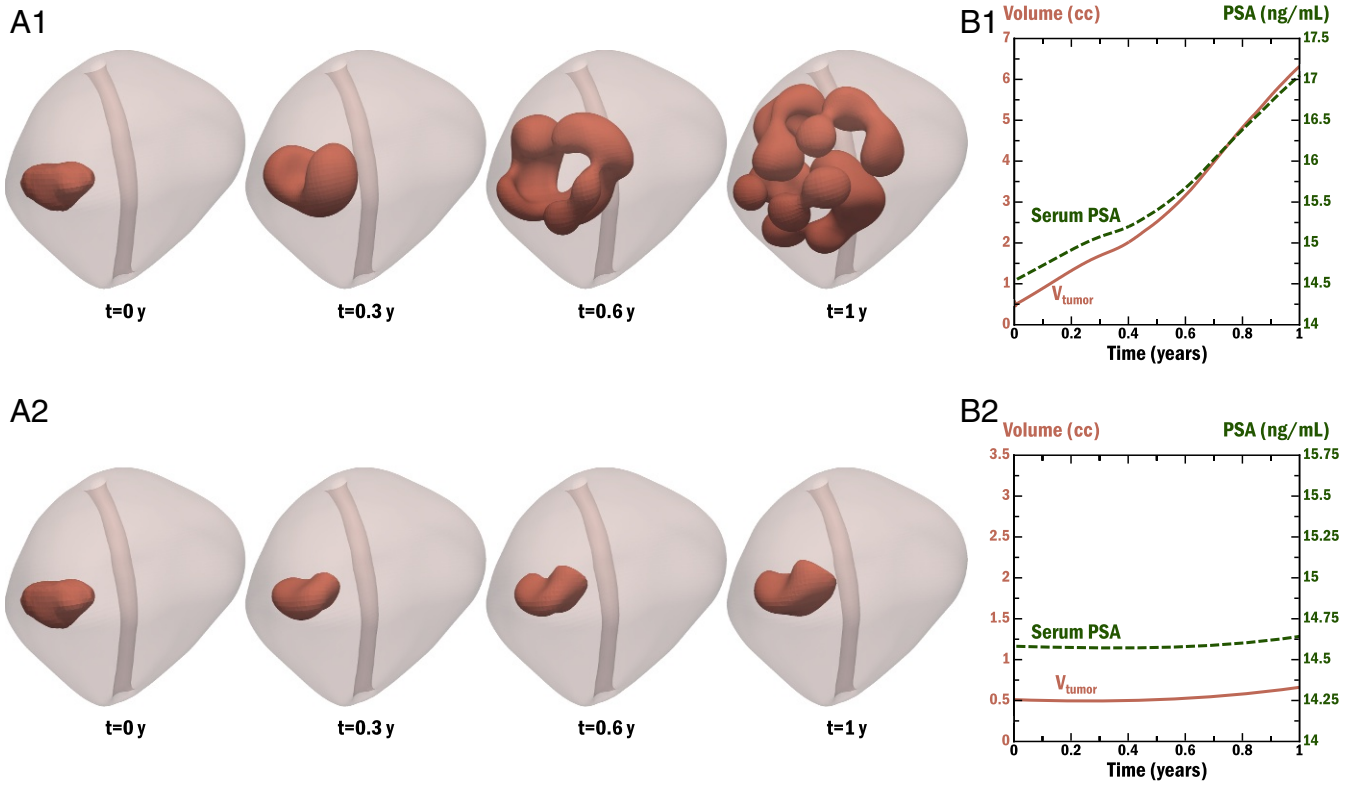

Fig. 4. Growth of the patient's tumor over 1 y without the influence of BPH (*A1* and *B1*) vs. considering the patient's history of benign prostatic enlargement (*A2* and *B2*). (*A1* and *A2*) Tumor growth over the original prostate geometry. (*B1* and *B2*) Time history of tumor volume (solid line) and serum PSA (dashed line).

PZ. The invasion of the CG was minimal and involved only the border with the PZ. The tumor growth rate was considerably lower than in the simulation without BPH and the final volume of the cancerous mass was 0.66 cc.

BPH globally dominated the deformation of the prostate by producing a volumetric expansion. The tumor produced a local swelling deformation that was noticeable on the external surface of the PZ. The urethra was displaced posteriorly to the patient's right and its diameter was practically unchanged. The deformation of the prostate caused by this combination of BPH and PCa produced maximum global displacements between 0.86 mm and 1.16 mm. These values were attained on the outer region of the tumor within the PZ. On the opposite side of the cancerous mass, the displacement field created by BPH within the CG was barely modified by the presence of the growing tumor.

The patient's history of BPH produced a highly compressive hydrostatic stress field in the prostate, ranging from −2.90 kPa to −2.20 kPa within the CG and from −0.60 kPa to −0.25 kPa within the PZ (*SI Appendix*, Fig. S4). The tumor contributed to increasing the hydrostatic stress in the PZ, reaching minima between −0.95 kPa and −0.70 kPa within the tumor and between −3.70 kPa and −2.90 kPa next to the CG border. BPH led to the accumulation of compressive stress all around the urethra (−6.20 kPa to −3.00 kPa) and tensile stress at the PZ tissue in the vicinity of the border between PZ and CG nearby the prostate external boundary (2.00–5.90 kPa).

The accumulated deformation by BPH also raised the Von Mises stress in the whole prostate (*SI Appendix*, Fig. S4). Within the CG, it ranged from 0.10 kPa at inner tissue, far from both the urethra and the external prostatic boundary, to higher values between 1.30 kPa and 1.80 kPa on the CG border. Within the PZ, the Von Mises stress was maximal on the CG surface, from 3.50 kPa to 5.00 kPa. The values of the Von Mises stress then decreased toward the prostate exterior boundary, where it ranged from 1.00 kPa to 2.50 kPa. The tumor locally increased the Von Mises stress, reaching 1.70–2.65 kPa on its outer lateral convex border within the PZ, within the tumor near its concave border, and surrounding the tumor tips in the craniocaudal direction. The intratumoral values were between 1.50 kPa and 2.20 kPa. The maximum Von Mises stress was observed along the urethra, especially along the anterior and posterior walls, ranging from 3.00 kPa to 8.00 kPa.

Discussion

In this work, we provide a mechanical explanation to understand why large prostates may exert a protective effect against PCa (10, 17–21). Using computer simulations based on a mechanically coupled mathematical model of organ-confined PCa, we show that a patient's history of BPH creates a deformational state that impedes tumor growth. Our results show that BPH promoted a highly compressive hydrostatic stress state within the CG and distorted the whole prostate, especially the PZ, hence increasing the Von Mises stress. The combination of this deformational state with the mechanical stress fields created by PCa impeded tumor growth, which showed a favorable pathological evolution characterized by a slow growing rate and the lack of invasive demeanor. This resulted in a smaller tumor volume, which is more likely to have a lower Gleason Score (47, 48) and hence be less aggressive. PCa was unable to grow beyond a certain thickness that would have motivated a shape instability toward a more invasive morphology, which would facilitate invasion of seminal vesicles or extracapsular extension. Instead, the deformational state of the prostate controlled the tumoral volume and permitted its development only along the less distorted and stressed directions. Increasing the Von Mises stress caused by both BPH and PCa in the prostatic tissue between the tumor and the prostate

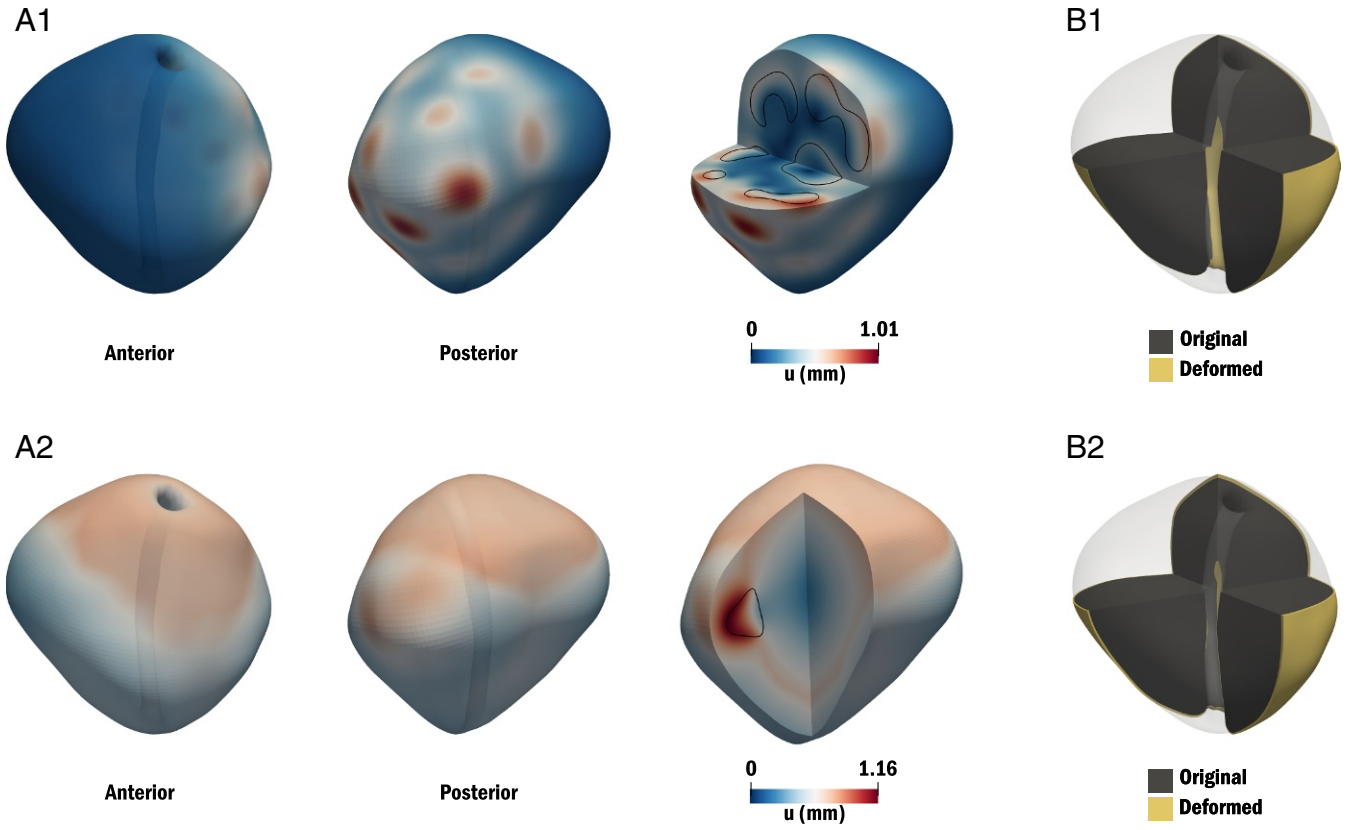

Fig. 5. Deformation of the prostate over 1 y produced by the patient's tumor without the influence of BPH (*A1* and *B1*) vs. considering the patient's history of benign prostatic enlargement (*A2* and *B2*). (*A1* and *A2*) Length of the displacement field vector over original anatomy at $t = 1$ y. The contour of the tumor is depicted with black curves. (*B1* and *B2*) Original and deformed geometries of the prostate at $t = 1$ y.

external boundary would also contribute to prevent the tumor from escaping the prostate.

The arrangement of tumor growth and geometry to its local mechanical environment was also previously observed and measured in in vitro experiments (25, 49). These studies along with our results highlight the major role of mechanical modulation of the shape and size of growing solid tumors, which are key pieces of information for clinical staging. Our results show that both hydrostatic stress and Von Mises stress developed significant values and actively regulated PCa growth. The mechanical states described by these stress measurements have been reported to impede tumor growth both experimentally and clinically (23–28, 32–34). When the BPH history was introduced in the simulations via $\boldsymbol{\sigma}^0$, we observed that the mechanical obstruction to tumor growth was mostly driven by high Von Mises stress accumulated in the PZ. Additionally, PCa growing in the CG would experience mechanical inhibition mostly driven by hydrostatic stress (*SI Appendix*, Fig. S4).

To calibrate and test our mechanically coupled mathematical model, we also studied the deformation of the prostate under the development of BPH and PCa. Overall, our results in terms of displacements and deformational features for BPH and PCa agree with previous studies in the medical literature (1, 42, 50). BPH produced the volumetric expansion of the prostate, with slightly higher displacements craniocaudally and anteroposteriorly at the basal level. The compression of the PZ dampened the displacement fields elsewhere. Simulation of BPH during several years would also produce the constriction of the urethra, as cued by the high hydrostatic stress in the surrounding CG.

PZ tumors deformed the outer posterior surface of the prostate, which would be noticed by a physician during a digital rectal examination (1). The CG tumor produced lower displacements and a uniform and subtle deformation on the posterior region of the prostate boundary. This is a common difficulty in detecting CG cancers during digital rectal examination. The constriction of the urethra along the segments circumvented by the tumor is likely to produce lower-urinary tract symptoms. Even though the displacements decreased after the shape instability, the volumes of the prostate, the CG, and the PZ were barely modified because the tumor grew faster with the fingered morphology. Consequently, milder displacement fields expanded over a broader volume of the prostate. PZ tumors grew slower because they accumulated higher compressive stress and the PZ was globally more distorted when the tumor grew against the prostate external surface and the CG border. PZ tumors adapted their shape to overcome those obstacles, favoring tumoral geometries that also anticipated the shape instability. We also observed that our model correctly reproduced the mechanical stress fields induced by a growing tumor as previously described in the literature (22–28).

However, our model presents some limitations that deserve further research. Our anatomic model of the prostate would benefit from a more precise segmentation of the internal prostatic zones accompanied by patient-specific mechanical characterization. Likewise, a spatially varying definition of the mechanical boundary conditions attending to the different tissues and organs surrounding the prostate would contribute to rendering more accurate predictions. These mechanical boundary conditions play a major role in the accumulation of hydrostatic stress in the prostate during the development of BPH, so future work should also focus on quantifying this influence to better understand the inhibitory mechanism presented herein. Our model would also benefit from a more accurate formulation for BPH (51–53) as well as for tumor growth and deformation (26, 33, 35,

36, 38). The mechanotransductive term to adjust tumor dynamics can be refined, for instance, by testing alternative formulations or differentiating how mechanical stress affects tumor mobility, proliferation, and apoptosis (25, 27, 33). To overcome the limitations of linear elasticity and obtain more accurate values of displacements and stresses future studies should explore a formulation accounting for geometric and material nonlinearities and investigate alternative constitutive equations for the prostate (28, 46, 54, 55). A poroelastic description of PCa growth would also help to study the effect of mechanical deformation on nutrient transport (26). This approach holds the potential to accurately investigate the heterogeneity of intratumoral metabolism or test patient-specific drug administration to the tumor in silico. To gain further knowledge on the mechanisms of PCa growth using our model, we believe it would be valuable to investigate the mathematical properties of the equations composing it, for example, analyzing solvability conditions, characterizing parameter spaces, and studying the well-posedness of the problem.

Finally, further validation using longitudinal series of clinical data is required to corroborate the BPH-induced mechanical inhibition of PCa. If validated, this mechanism may produce an important shift in the clinical management of BPH. Our results advise performing a comprehensive examination of the prostate in men without PCa before prescribing BPH treatments or drugs aimed at reducing the CG volume. Likewise, our results recommend a close follow-up of those patients with PCa receiving these sorts of BPH drugs. Otherwise, the prostate volumetric decrease could hazardously lower the mechanical stress fields created by BPH and hence reduce their mechanical restraint on PCa growth. Indeed, this could partially explain the higher proportion of more aggressive cancers in the finasteride arm of the Prostate Cancer Prevention Trial (56), arguably the most controversial result of this milestone study on chemoprevention of PCa (14, 18–20). Our research also calls for further courses of treatment in alleviating BPH symptoms while maintaining a significant stress level within the prostate for protection against PCa. In the future, we intend to address this issue by extending our model to incorporate the effect of drugs causing a prostate volume decrease, such as dutasteride and finasteride (1, 56). Additionally, we think that our model could be exploited to improve the current technologies for deformable registration of medical images (42) by providing a theory for the evolution of BPH and PCa. The resulting algorithms would be of much interest for several applications within the clinical management of PCa on a tissue-scale, patient-specific basis, such as the accurate follow-up of tumor growth during active surveillance or the precise planning of surgery and other treatments (39). Such technology could also help to detect PCa based on the deformation of the prostate boundaries and the internal borders between prostatic regions (44, 57). Additionally, it could guide biopsies to better stage and diagnose PCa. Comparing the predictions of the model with new images and clinical data could also help to discern whether the tumor is progressing toward a more malignant behavior and to make clinical decisions accordingly (39).

Materials and Methods

Patient Data. Anonymized patient data were obtained from the public repository for PCa imaging data at the Initiative for Collaborative Computer Vision Benchmarking website (i2cvb.github.io/) (58). Institutional review board approval and informed consent were not required for this study. We used the multiparametric MR image dataset obtained with a 3.0 Tesla Siemens Magnetom Trio TIM scanner. Patient cohort description and details on data acquisition have been previously described (59). For each biopsy-confirmed patient, this database includes T2-weighted MR images; dynamic contrast enhanced MR images; diffusion-weighted MR images; MR spectroscopic images; apparent diffusion coefficient maps; and the segmentations of the prostate, the PZ, the CG, and the tumor by an experienced radiologist. For this research, we selected a patient aged 54 y at MR date who had a large prostate of 52.81 cc harboring a localized tumor in the PZ.

Mathematical Model. Our modeling philosophy aims at developing tumor growth models based on key phenomena and featuring a limited number of representative parameters (30). This approach holds the potential for precise heterogeneous parameterization using available longitudinal clinical and imaging data from patients and has proved successful in reproducing and predicting various types of tumor growth (30, 32–34). As a preliminary step in this direction, here we developed a mechanically coupled model for patient-specific, organ-confined PCa growth and we leveraged it to perform a study on the mechanical interaction between PCa and BPH using literature data for parameter calibration.

Our model is described by the following equations:

$$\frac{\partial \phi}{\partial t} = M\left(D_\phi \Delta\phi - \frac{1}{\tau}\frac{\mathrm{d}F(\phi)}{\mathrm{d}\phi} + \chi s - A\phi\right) \quad [1]$$

$$\frac{\partial s}{\partial t} = D_s \Delta s + S - \delta\phi - \gamma_s s \quad [2]$$

$$\frac{\partial p}{\partial t} = D_p \Delta p + \alpha_h(1-\phi) + \alpha_c\phi - \gamma_p p \quad [3]$$

$$\nabla \cdot \boldsymbol{\sigma} = \mathbf{0}. \quad [4]$$

Eqs. **1**–**3** come from our previous model of organ-confined PCa growth (39, 40). Eq. **1** describes tumor dynamics using the phase-field method (41). The order parameter ϕ takes values from 0 in healthy tissue to 1 within tumoral regions, showing a thin diffuse interface in between. $F(\phi) = 16\phi^2(1-\phi)^2$ is a double-well potential, which enables the stable coexistence of healthy and cancerous tissue in our model. The last two terms in Eq. **1** describe nutrient-driven growth and apoptosis (i.e., programed cell death), respectively. We consider that tumor growth is driven by a generic nutrient s that follows reaction–diffusion dynamics in Eq. **2**. The reactive terms in Eq. **2** are the nutrient supply, the consumption of nutrient by the tumor, and a natural decay, respectively. Eq. **3** describes the reaction–diffusion dynamics of tissue PSA p, defined as the serum PSA concentration leaked to the bloodstream per unit volume of prostatic tissue (39). In Eq. **3**, we consider that healthy tissue and cancerous tissue produce p at rates α_h and α_c, respectively, and the last term is a natural decay.

The mechanical stress fields generated by a growing tumor have been shown to slow down its dynamics (23–28). Previous clinically oriented, mechanically coupled models of tumor growth have incorporated this phenomenon by means of a coefficient that exponentially decreases cell mobility or net cell proliferation as mechanical stress fields intensify (30, 32–34). Following a similar strategy, in Eq. **1** we modeled the mechanically induced inhibition of tumor growth throughout coefficient M, which we define in Eq. **5**. Mechanical stress can be decomposed as the sum of hydrostatic stress σ_h (defined in Eq. **6**), which tends to change the volume of the stressed body, and deviatoric stress, which tends to distort it (46). The Von Mises stress σ_v (46) (defined in Eq. **7**) is a good measure of the distortional strain energy around the tumor that has been widely adopted in mechanically coupled models (32–34). However, σ_v is insensitive to hydrostatic stress, which better describes the natural stress state within a growing region of tissue, such as a tumor or the CG developing BPH (23, 24, 26). Hydrostatic stress is also bound to increase globally during these growth processes because the prostate is a confined organ (1). Therefore, we propose to combine σ_v and the hydrostatic stress σ_h (46) in the definition of M following a similar approach to that of multiaxial stress-based failure criteria,

$$M = e^{-\beta_1(\sigma_v + \beta_2|\sigma_h|)}, \quad [5]$$

where

$$\sigma_h = \frac{1}{3}\boldsymbol{\sigma} : \mathbf{I} = \frac{1}{3}(\sigma_{11} + \sigma_{22} + \sigma_{33}), \quad [6]$$

$$\sigma_v = \left(\sigma_{11}^2 + \sigma_{22}^2 + \sigma_{33}^2 - \sigma_{11}\sigma_{22} - \sigma_{22}\sigma_{33} - \sigma_{33}\sigma_{11} + 3\left(\sigma_{12}^2 + \sigma_{23}^2 + \sigma_{13}^2\right)\right)^{1/2}, \quad [7]$$

where σ_{ij} with $i, j = 1, 2, 3$ are the components of the stress tensor $\boldsymbol{\sigma}$, $\mathbf{I}$ is the second-order identity tensor, and β_1 and β_2 are constants that were adjusted to match the experimental and clinical results of previous studies on tumor growth (23–28, 32–34). We use the absolute value of the hydrostatic stress because both growth-induced compressive and tensile solid stresses have been shown to impede tumor dynamics at tissue scale in vivo (23, 24).

We assume that PCa and BPH show sufficiently slow rates (1) to neglect the inertial effects in the deformation of prostatic tissue. Hence, Eq. **4**

describes mechanical equilibrium as a quasistatic process. Linear elasticity has been widely accepted to model mechanical equilibrium in living tissue subjected to slow processes over short time scales ($t \sim 1$ y) (32–38, 46). Hence, this paradigm provides a simple mechanical framework to compute the stresses in Eq. **5** and perform our qualitative study on the mechanical influence of BPH on PCa. The prostate is an histologically heterogeneous organ: While the CG has a higher and denser stromal component, the PZ has more abundant glandular elements with sparsely interwoven smooth muscle (1, 5, 6). Benign enlargement of the prostate tends to make the CG denser and more compact (1, 7). Therefore, the CG is normally stiffer than the PZ in patients with PCa and/or BPH (42–45). The growing tumor induces an internal compressive hydrostatic stress and exerts outward forces acting on the tumor border (22, 24), so we modeled the tumor mass effect as

$$p_{tumor} = -\kappa\phi. \qquad [8]$$

This assumes that κ is the magnitude of a constant compressive pressure, which is admissible over short simulation times (32–34, 36, 37). Volumetric growth due to BPH is usually modeled with an exponential function, but the slow growth rates justify a linear approximation over periods $\Delta t \sim 1$–10 y (51–53). Hence, we modeled BPH as a linearly growing pressure acting only on the CG,

$$p_{BPH} = -K\varrho\frac{g\Delta t}{V_{MRI}}\mathcal{H}_{CG}(\mathbf{x}), \qquad [9]$$

where K is the bulk modulus, g is the estimated linear volumetric growth rate of the prostate due to BPH at MR date, V_{MRI} is the volume of the prostate as measured on T2-weighted MRI, Δt is the time passed since the date of MRI, and $\mathcal{H}_{CG}(\mathbf{x})$ is a Heaviside function with value 1 in the CG and 0 elsewhere. The parameter ϱ adjusts the value of the pressure p_{BPH} to obtain the estimated CG growth rate. Taking all of the considerations above, we model prostatic tissue as a linear elastic, heterogeneous, isotropic material whose constitutive equation is given by

$$\boldsymbol{\sigma} = \lambda(\boldsymbol{\nabla}\cdot\mathbf{u})\mathbf{I} + 2\mu\boldsymbol{\nabla}^s\mathbf{u} - \kappa\phi\mathbf{I} - K\varrho\frac{g\Delta t}{V_{MRI}}\mathcal{H}_{CG}(\mathbf{x})\mathbf{I}, \qquad [10]$$

where $\boldsymbol{\sigma}$ is the stress tensor, λ and μ are the Lamé constants, $\mathbf{u}$ is the displacement vector, and $\mathbf{x}$ is the position vector. The segmentation of CG and PZ was extracted from our patient's imaging data and mapped over the quadrature points to define heterogeneous material properties (Fig. 1).

We computed tumor volume V_ϕ and serum PSA P as (39)

$$V_\phi = \int_\Omega \phi d\Omega \qquad P = \int_\Omega p d\Omega, \qquad [11]$$

where Ω is the prostate segmented on the patient's MR images.

Because we are focusing on localized PCa, we imposed zero-valued Dirichlet conditions for ϕ all over the prostate boundary $\partial\Omega$. We set natural boundary conditions for s and p. The confinement of the prostate within the pelvic area (1) was modeled with Winkler-inspired boundary conditions on the external surface of the prostate, while free displacement was enabled along the urethra; i.e.,

$$\boldsymbol{\sigma}\mathbf{n} = -k_w\mathbf{u} \quad \text{in } \partial\Omega|_{exterior} \qquad \boldsymbol{\sigma}\mathbf{n} = \mathbf{0} \quad \text{in } \partial\Omega|_{urethra}, \qquad [12]$$

where $\mathbf{n}$ is the outer normal vector to $\partial\Omega$ and k_w is constant.

The initial condition of the phase field, ϕ_0, was an L^2 projection of the tumor segmentation extracted from the patient's T2-weighted MR images and mapped over quadrature points or was artificially modeled with an L^2-projected hyperbolic tangent field. The initial conditions for s and p were approximated with linear functions based on ϕ_0 (40). Linear elasticity allows us to apply the principle of superposition and set zero-valued initial conditions for the displacements; i.e., $\mathbf{u}_0 = \mathbf{0}$. This means that we are computing only the displacements produced since the MR date.

To study how BPH mechanically influences PCa growth, we estimated the stress state $\boldsymbol{\sigma}^0$ caused by the history of BPH before the detection of PCa at MR date and leveraged it as a prestress state to compute M in Eq. **1**. Hence, for this purpose, $\boldsymbol{\sigma} = \boldsymbol{\sigma}^0 + \boldsymbol{\sigma}^1$, where $\boldsymbol{\sigma}^1$ are the stresses developed since the detection of PCa at MR date. To estimate $\boldsymbol{\sigma}^0$, we assumed that the volume of the patient's prostate was 20 cc at age 40 y (1, 3) and leveraged Eq. **4** with a negative value for g and $\Delta t = 14$ y to approximate the undeformed, healthy state of our patient's prostate according to the standard anatomical features (1). Because we are using linear elasticity, it suffices to reverse the sign of the obtained displacements to yield $\mathbf{u}^0$ and then approximate $\boldsymbol{\sigma}^0$ as

$$\boldsymbol{\sigma}^0 = \lambda\left(\boldsymbol{\nabla}\cdot\mathbf{u}^0\right)\mathbf{I} + 2\mu\boldsymbol{\nabla}^s\mathbf{u}^0 - K\varrho\frac{g\Delta t^0}{V_{MRI}}\mathcal{H}_{CG}(\mathbf{x})\mathbf{I}, \qquad [13]$$

where g is now positive and $\Delta t^0 = 14$ y.

Parameter selection for Eqs. **1–3** has been previously discussed (39) and it is provided in Table 1. We set the values of the Young modulus of PZ and CG to $E_{PZ} = 3$ kPa and $E_{CG} = 6$ kPa, respectively (42–45). Because living soft tissues have a high content of water (34, 37, 42), we set the Poisson coefficients $\nu_{PZ} = \nu_{CG} = 0.40$. We empirically calibrated $\beta_1 = 0.80$ 1/kPa and $\beta_2 = 1.50$ in agreement with the experimental and clinical observations reported in previous studies on tumor growth (23–28, 32–34). We selected $\kappa = 2.50$ kPa to produce displacements in the order of 1 mm. The analysis of BPH and PCa deformation and the computation of the stress fields $\boldsymbol{\sigma}^0$ rendered $g = 2.34$ cc/y, $\varrho = 2.78$, and $k_w = 0.23$ kPa/mm. These values for g and ϱ reasonably agree with previous observations in the literature for our patient characteristics (1, 3, 50–53).

Finally, we acknowledge that linear elasticity is an acceptable simplification for studies featuring small strains and rotations and that the strain values in the simulations shown in Figs. 3–5 are somewhat outside the admissible range for linear elasticity in a few localized regions along the tumor interface. Additionally, the prestress $\boldsymbol{\sigma}^0$ is just a gross estimate of the stress state in the prostate due to the history of BPH previous to PCa detection at MR. However, we are using the stresses only to compute the mechanotransductive factor to adjust tumor dynamics. This study also features other major sources of uncertainty beyond linear elasticity, such as prostate and tumor segmentation, the PCa model itself, or the mechanical boundary conditions. Still, our predictive simulations still qualitatively reproduce the inhibiting effect on tumor growth caused by the tumor mass effect and a history of BPH before PCa detection. To verify the validity of the use of linear kinematic theory, we computed the symmetrical and skew-symmetrical components of the displacement gradient with respect to the initial configuration and determined that they were sufficiently small that their products were not substantial compared with the linear terms and, in particular, that the skew-symmetric components were negligible everywhere. Consequently, we feel confident that the computed results provide physically meaningful information.

Numerical Methods. Since tumor growth and BPH are modeled as quasistatic processes, we adopted a staggered approach to solve the equations in our mathematical model. We calculated tumor growth at every time step, but we updated the displacements only every two time steps. We performed spatial discretization by means of a standard isogeometric Bubnov–Galerkin approach using a 3D C^1 quadratic nonuniform rational B-spline (NURBS) space (39, 40, 60–62). Temporal integration in the tumor growth problem was carried out with the generalized-α method (63, 64). This technique led to a nonlinear problem in each time step, which we linearized using the Newton–Raphson method. The resulting linear system was solved using the generalized minimal residual method (GMRES) algorithm (65) with a diagonal preconditioner. We also used the preconditioned GMRES algorithm to solve the quasistatic elastic problem. We chose a constant time step of

Table 1. List of parameters in Eqs. 1–3

Parameter	Notation	Value
Diffusivity of the phase field	D_ϕ	200 mm^2/y
Time scale for the phase field	τ	0.01 y
Nutrient-induced tumor growth rate	χ	600 L/(g· y)
Apoptosis rate	A	600 1/y
Nutrient diffusivity	D_s	$5.47 \cdot 10^3$ mm^2/y
Nutrient supply	S	2.70 g/(L· d)
Nutrient consumption rate	δ	2.75 g/(L· d)
Nutrient natural decay rate	γ_s	1,000 1/y
Tissue PSA diffusivity	D_p	200 mm^2/y
Healthy tissue PSA production rate	α_h	6.25 (ng/mL)/(cc·y)
Tumoral tissue PSA production rate	α_c	$\alpha_c = 15\alpha_h$
Tissue PSA natural decay rate	γ_p	100 1/y

0.002 y and the parameters in the generalized-α method were set as in previous studies (40, 66).

Visualization. We used ParaView (67) to visualize and explore the results of our simulations. We used the isovolume $\phi \geq 0.5$ to represent the tumor, which permitted us to study the evolution of PCa morphologies. From the C^1-continuous basis, we computed the stress fields pointwise. We identified regions of interest for the stress fields in the simulations and isolated them using appropriate geometric filters in ParaView. The stresses reported in the text correspond to the range of values that best describe the stress field in each region of interest.

Construction of the Prostate Mesh. Multiple methodologies permit the construction of solid anatomic NURBS models (68, 69). Because the geometries of the prostate and a solid torus are topologically equivalent, we leveraged a parametric mapping algorithm (70, 71) to deform a torus solid NURBS model to match with a patient-specific prostate surface model. We used 3DSlicer (72) to generate a triangular surface model of the prostate from the contours of the organ and the urethra drawn on the T2-weighted MR images, using the provided prostate segmentation as guidance. The resulting surface was smoothed in MeshLab (73).

The original torus and prostate NURBS meshes were discretized with $32 \times 32 \times 8$ elements along the toroidal direction, the cross-section circumferential direction, and the cross-section radial direction, respectively. We globally refined the prostate mesh to $256 \times 256 \times 64$ elements, using standard knot insertion (61) to perform our simulations with a good level of accuracy.

ACKNOWLEDGMENTS. We thank Pablo Orosa-Iglesias (Universidade da Coruña, Spain) for his valuable help in the construction of the prostate mesh. We acknowledge the Centro de Supercomputación de Galicia (Santiago de Compostela, Spain) for providing high-performance computing resources that contributed to the results presented in this paper. G.L., P.D.-F., and H.G. were partially supported by the European Research Council (Contract 307201) and Xunta de Galicia (Consellería de Cultura, Educación e Ordenación Universitaria). G.L. and A.R. were partially supported by Fondazione Cariplo–Regione Lombardia through the project "Verso nuovi strumenti di simulazione super veloci ed accurati basati sull'analisi isogeometrica," within the program RST–rafforzamento.

1. Wein AJ, Kavoussi LR, Novick AC, Partin AW, Peters CA (2012) *Campbell-Walsh Urology: Expert Consult Premium Edition: Enhanced Online Features and Print, 4-Volume Set* (Elsevier Saunders, Philadelphia), 10th Ed.
2. Ferlay J, et al. (2015) Cancer incidence and mortality worldwide: Sources, methods and major patterns in GLOBOCAN 2012. *Int J Cancer* 136:E359–E386.
3. Berry SJ, Coffey DS, Walsh PC, Ewing LL (1984) The development of human benign prostatic hyperplasia with age. *J Urol* 132:474–479.
4. Coakley FV, Hricak H (2000) Radiologic anatomy of the prostate gland: A clinical approach. *Radiol Clin* 38:15–30.
5. Villeirs GM, Verstraete KL, De Neve WJ, De Meerleer GO (2005) Magnetic resonance imaging anatomy of the prostate and periprostatic area: A guide for radiotherapists. *Radiother Oncol* 76:99–106.
6. De Visschere PJL, et al. (2017) Multiparametric magnetic resonance imaging characteristics of normal, benign and malignant conditions in the prostate. *Eur Radiol* 27:2095–2109.
7. Noworolski SM, Vigneron DB, Chen AP, Kurhanewicz J (2008) Dynamic contrast-enhanced MRI and MR diffusion imaging to distinguish between glandular and stromal prostatic tissues. *Magn Reson Imaging* 26:1071–1080.
8. Alcaraz A, Hammerer P, Tubaro A, Schröder FH, Castro R (2009) Is there evidence of a relationship between benign prostatic hyperplasia and prostate cancer? Findings of a literature review. *Eur Urol* 55:864–875.
9. Ørsted DD, Bojesen SE (2013) The link between benign prostatic hyperplasia and prostate cancer. *Nat Rev Urol* 10:49–54.
10. Chen ME, Troncoso P, Johnston D, Tang K, Babaian RJ (1999) Prostate cancer detection: Relationship to prostate size. *Urology* 53:764–768.
11. Werahera PN, et al. (2012) Optimization of prostate cancer diagnosis by increasing the number of core biopsies based on gland volume. *Int J Clin Exp Pathol* 5:892–899.
12. Gorski A, et al. (2015) Accuracy of magnetic resonance imaging/ultrasound fusion targeted biopsies to diagnose clinically significant prostate cancer in enlarged compared to smaller prostates. *J Urol* 194:669–673.
13. Ung JO, San Francisco IF, Regan MM, DeWolf WC, Olumi AF (2003) The relationship of prostate gland volume to extended needle biopsy on prostate cancer detection. *J Urol* 169:130–135.
14. Kulkarni GS, et al. (2006) Evidence for a biopsy derived grade artifact among larger prostate glands. *J Urol* 175:505–509.
15. Diaz AW, et al. (2013) Can magnetic resonance-ultrasound fusion biopsy improve cancer detection in enlarged prostates? *J Urol* 190:2020–2025.
16. Scattoni V, et al. (2008) Initial extended transrectal prostate biopsy—are more prostate cancers detected with 18 cores than with 12 cores? *J Urol* 179:1327–1331.
17. Freedland SJ, et al. (2005) Prostate size and risk of high-grade, advanced prostate cancer and biochemical progression after radical prostatectomy: A search database study. *J Clin Oncol* 23:7546–7554.
18. Kassouf W, et al. (2007) Effect of prostate volume on tumor grade in patients undergoing radical prostatectomy in the era of extended prostatic biopsies. *J Urol* 178:111–114.
19. Briganti A, et al. (2007) Prostate volume and adverse prostate cancer features: Fact not artifact. *Eur J Cancer* 43:2669–2677.
20. Newton MR, et al. (2010) Smaller prostate size predicts high grade prostate cancer at final pathology. *J Urol* 184:930–937.
21. Hong SK, Poon BY, Sjoberg DD, Scardino PT, Eastham JA (2014) Prostate size and adverse pathologic features in men undergoing radical prostatectomy. *Urology* 84:153–157.
22. Gordon V, et al. (2003) Measuring the mechanical stress induced by an expanding multicellular tumor system: A case study. *Exp Cell Res* 289:58–66.
23. Stylianopoulos T, et al. (2013) Coevolution of solid stress and interstitial fluid pressure in tumors during progression: Implications for vascular collapse. *Cancer Res* 73:3833–3841.
24. RakeshJain K, JohnMartin D, Stylianopoulos T (2014) The role of mechanical forces in tumor growth and therapy. *Annu Rev Biomed Eng* 16:321–346.
25. Helmlinger G, Netti PA, Lichtenbeld HC, Melder RJ, Jain RK (1997) Solid stress inhibits the growth of multicellular tumor spheroids. *Nat Biotechnol* 15:778–783.
26. Roose T, Netti PA, Munn LL, Boucher Y, Jain RK (2003) Solid stress generated by spheroid growth estimated using a linear poroelasticity model. *Microvasc Res* 66:204–212.
27. Cheng G, Tse J, Jain RK, Munn LL (2009) Micro-environmental mechanical stress controls tumor spheroid size and morphology by suppressing proliferation and inducing apoptosis in cancer cells. *PLoS One* 4:e4632.
28. Voutouri C, Mpekris F, Papageorgis P, Odysseos AD, Stylianopoulos T (2014) Role of constitutive behavior and tumor-host mechanical interactions in the state of stress and growth of solid tumors. *PLoS One* 9:e104717.
29. Anderson ARA, Quaranta V (2008) Integrative mathematical oncology. *Nat Rev Cancer* 8:227–234.
30. Yankeelov TE, et al. (2013) Clinically relevant modeling of tumor growth and treatment response. *Sci Transl Med* 5:187ps9.
31. Oden JT, et al. (2016) Toward predictive multiscale modeling of vascular tumor growth. *Arch Comput Methods Eng* 23:735–779.
32. Weis JA, et al. (2015) Predicting the response of breast cancer to neoadjuvant therapy using a mechanically coupled reaction–diffusion model. *Cancer Res* 75:4697–4707.
33. Lima E, et al. (2017) Selection and validation of predictive models of radiation effects on tumor growth based on noninvasive imaging data. *Comput Methods Appl Mech Eng* 327:277–305.
34. Weis JA, Miga MI, Yankeelov TE (2017) Three-dimensional image-based mechanical modeling for predicting the response of breast cancer to neoadjuvant therapy. *Comput Methods Appl Mech Eng* 314:494–512.
35. Chen X, Summers RM, Yao J (2013) Kidney tumor growth prediction by coupling reaction-diffusion and biomechanical model. *IEEE Trans Biomed Eng* 60:169–173.
36. Liu Y, et al. (2014) Patient specific tumor growth prediction using multimodal images. *Med Image Anal* 18:555–566.
37. Clatz O, et al. (2005) Realistic simulation of the 3-D growth of brain tumors in MR images coupling diffusion with biomechanical deformation. *IEEE Trans Med Imaging* 24:1334–1346.
38. Hogea C, Davatzikos C, Biros G (2008) An image-driven parameter estimation problem for a reaction–diffusion glioma growth model with mass effects. *J Math Biol* 56:793–825.
39. Lorenzo G, et al. (2016) Tissue-scale, personalized modeling and simulation of prostate cancer growth. *Proc Natl Acad Sci USA* 113:E7663–E7671.
40. Lorenzo G, Scott MA, Tew K, Hughes TJR, Gomez H (2017) Hierarchically refined and coarsened splines for moving interface problems, with particular application to phase-field models of prostate tumor growth. *Comput Methods Appl Mech Eng* 319:515–548.
41. Qin RS, Bhadeshia HK (2010) Phase field method. *Mater Sci Tech* 26:803–811.
42. Bharatha A, et al. (2001) Evaluation of three-dimensional finite element-based deformable registration of pre- and intraoperative prostate imaging. *Med Phys* 28:2551–2560.
43. Zhai L, et al. (2010) Characterizing stiffness of human prostates using acoustic radiation force. *Ultrason Imaging* 32:201–213.
44. Wang Yi, et al. (2016) Patient-specific deformation modelling via elastography: Application to image-guided prostate interventions. *Scientific Rep* 6:27386.
45. Rouvière O, et al. (2017) Stiffness of benign and malignant prostate tissue measured by shear-wave elastography: A preliminary study. *Eur Radiol* 27:1858–1866.
46. Irgens F (2008) *Continuum Mechanics* (Springer, Berlin).
47. Partin AW, et al. (1990) Prostate specific antigen in the staging of localized prostate cancer: Influence of tumor differentiation, tumor volume and benign hyperplasia. *J Urol* 143:747–752.
48. Turkbey B, et al. (2012) Correlation of magnetic resonance imaging tumor volume with histopathology. *J Urol* 188:1157–1163.
49. Mills KL, Kemkemer R, Rudraraju S, Garikipati K (2014) Elastic free energy drives the shape of prevascular solid tumors. *PLoS One* 9:e103245.

50. Cao N, et al. (2017) The characteristics of the transitional zone in prostate growth with age. *Urology* 105:136–140.
51. Lieber MM, et al. (2010) Natural history of benign prostatic enlargement: Long-term longitudinal population-based study of prostate volume doubling times. *BJU Int* 105:214–219.
52. Roehrborn CG, et al. (2000) Serum prostate specific antigen is a strong predictor of future prostate growth in men with benign prostatic hyperplasia. *J Urol* 163:13–20.
53. Williams AM, et al. (1999) Prostatic growth rate determined from MRI data: Age-related longitudinal changes. *J Androl* 20:474–480.
54. Goriely A (2017) *The Mathematics and Mechanics of Biological Growth*, Interdisciplinary Applied Mathematics (Springer, New York).
55. Menzel A, Kuhl E (2012) Frontiers in growth and remodeling. *Mech Res Commun* 42:1–14.
56. Thompson IM, et al. (2003) The influence of finasteride on the development of prostate cancer. *N Engl J Med* 349:215–224.
57. Rusu M, et al. (2017) Computational imaging reveals shape differences between normal and malignant prostates on MRI. *Sci Rep* 7:41261.
58. Lemaître G, et al. (2015) Computer-aided detection and diagnosis for prostate cancer based on mono and multi-parametric MRI: A review. *Comput Biol Med* 60:8–31.
59. Lemaître G (2016) Computer-aided diagnosis for prostate cancer using multi-parametric magnetic resonance imaging. PhD thesis (Universitat de Girona, Girona, Spain).
60. Hughes TJR, Cottrell JA, Bazilevs Y (2005) Isogeometric analysis: CAD, finite elements, NURBS, exact geometry and mesh refinement. *Comp Methods Appl Mech Eng* 194:4135–4195.
61. Cottrell JA, Hughes TJR, Bazilevs Y (2009) *Isogeometric Analysis: Toward Integration of CAD and FEA* (Wiley, Chichester, UK).
62. Piegl LA, Tiller W (1996) *The NURBS Book*, *Monographs in Visual Communication* (Springer, Berlin).
63. Chung J, Hulbert GM (1993) A time integration algorithm for structural dynamics with improved numerical dissipation: The generalized-α method. *J Appl Mech* 60:371–375.
64. Jansen KE, Whiting CH, Hulbert GM (2000) A generalized-α method for integrating the filtered Navier–Stokes equations with a stabilized finite element method. *Comp Methods Appl Mech Eng* 190:305–319.
65. Saad Y, Schultz MH (1986) Gmres: A generalized minimal residual algorithm for solving nonsymmetric linear systems. *SIAM J Sci Stat Comput* 7:856–869.
66. Gómez H, Calo VM, Bazilevs Y, Hughes TJR (2008) Isogeometric analysis of the Cahn-Hilliard phase-field model. *Comp Methods Appl Mech Eng* 197:4333–4352.
67. Ayachit U (2015) *The ParaView Guide (Full Color Version): A Parallel Visualization Application* (Kitware, Inc., New York).
68. Zhang YJ (2016) *Geometric Modeling and Mesh Generation from Scanned Images*, *Chapman & Hall/CRC Mathematical and Computational Imaging Sciences Series* (Chapman and Hall/CRC, Boca Raton, FL).
69. Zhang Y, Bazilevs Y, Goswami S, Bajaj CL, Hughes TJR (2007) Patient-specific vascular NURBS modeling for isogeometric analysis of blood flow. *Comput Methods Appl Mech Eng* 196:2943–2959.
70. Floater MS, Hormann K (2005) Surface parameterization: A tutorial and survey. *Advances in Multiresolution for Geometric Modelling*, eds Dodgson NA, Floater MS, Sabin MA (Springer, Berlin), pp 157–186.
71. Zhang Y, Wang W, Hughes TJR (2012) Solid T-spline construction from boundary representations for genus-zero geometry. *Comput Methods Appl Mech Eng* 249:185–197.
72. Fedorov A, et al. (2012) 3D Slicer as an image computing platform for the Quantitative Imaging Network. *Magn Reson Imaging* 30:1323–1341.
73. Cignoni P, et al. (2008) MeshLab: An open-source mesh processing tool. *Eurographics Italian Chapter Conference*, eds Scarano V, Chiara RD, Erra U (Eurographics Assoc., Geneve, Switzerland).